OPEN ACCESS
OPUS AUGSBURG

Universität Augsburg
Universitätsbibliothek

Molecular imaging of tumors with nanobodies and antibodies: timing and dosage are crucial factors for improved in vivo detection

B. Bannas, A. Lenz, V. Kunick, L. Well, W. Fumey, B. Rissiek, F. Haag, J. Schmidt, K. Schütze, A. Eichhoff, Martin Trepel, G. Adam, H. Ittrich, F. Koch-Nolte

Angaben zur Veröffentlichung / Publication details:

Bannas, B., A. Lenz, V. Kunick, L. Well, W. Fumey, B. Rissiek, F. Haag, et al. 2015. "Molecular imaging of tumors with nanobodies and antibodies: timing and dosage are crucial factors for improved in vivo detection." *Contrast Media & Molecular Imaging* 10 (5): 367–78. https://doi.org/10.1002/cmmi.1637.

Nutzungsbedingungen / Terms of use: **CC BY 4.0**

Dieses Dokument wird unter folgenden Bedingungen zur Verfügung gestellt: / This document is made available under these conditions:
CC-BY 4.0: Creative Commons: Namensnennung
Weitere Informationen finden Sie unter: / For more information see:
https://creativecommons.org/licenses/by/4.0/deed.de

CONTRAST MEDIA & MOLECULAR IMAGING

Received: 3 September 2014, Revised: 23 January 2015, Accepted: 3 February 2015, Published online in Wiley Online Library: 27 April 2015

(wileyonlinelibrary.com) DOI: 10.1002/cmmi.1637

Molecular imaging of tumors with nanobodies and antibodies: Timing and dosage are crucial factors for improved *in vivo* detection

Peter Bannas[a]*†, Alexander Lenz[a,b†], Valentin Kunick[a,b], Lennart Well[a,b], William Fumey[a,b], Björn Rissiek[b,c], Friedrich Haag[b], Joanna Schmid[a,b], Kerstin Schütze[a,b], Anna Eichhoff[b], Martin Trepel[d], Gerhard Adam[a], Harald Ittrich[a] and Friedrich Koch-Nolte[b]

The utility of nanobodies and conventional antibodies for *in vivo* imaging is well known, but optimum dosing and timing schedules for one versus the other have not been established. We aimed to improve specific tumor imaging *in vivo* with nanobodies and conventional antibodies using near-infrared fluorescence (NIRF) imaging. We used ARTC2 expressed on lymphoma cells as a model target antigen. ARTC2-specific nanobody s+16a and conventional antibody Nika102 were labeled with NIRF-dye AF680. *In vivo* NIRF-imaging of ARTC2-positive and ARTC2-negative xenografts was performed over 24 h post-injection of 5, 10, 25, or 50 μg of each conjugate. Specific target-binding and tissue-penetration were verified by NIRF imaging *ex vivo*, flow cytometry and fluorescence microscopy. NIRF-imaging of s+16a^{680} *in vivo* revealed a six times faster tumor accumulation than of Nika102^{680}. Using 50 μg of s+16a^{680} increased the specific signals of ARTC2-positive tumors without increasing background signals, allowing a tumor-to-background (T/B) ratio of 12.4 ± 4.2 within 6 h post-injection. Fifty micrograms of Nika102^{680} increased specific signals of ARTC2-positive tumors but also of ARTC2-negative tumors and background, thereby limiting the T/B ratio to 6.1 ± 2.0. Ten micrograms of Nika102^{680} only slightly reduced specific tumor signals but dramatically reduced background signals. *Ex vivo* analyses confirmed a faster and deeper tumor penetration with s+16a^{680}. Using nanobody s+16a allowed same-day imaging with a high T/B ratio, whereas antibody Nika102 gave optimal imaging results only 24 h post injection. Nanobody s+16a required a high dose, whereas antibody Nika102 had the best T/B-ratio at a low dose. Therefore, timing and dosage should be addressed when comparing nanobodies and conventional antibodies for molecular imaging purposes. **Copyright © 2015 John Wiley & Sons, Ltd.**

Additional supporting information may be found in the online version of this article at the publisher's web site.

Keywords: Nanobody; antibody; VHH; fluorescence imaging; molecular imaging; xenograft; animal model

1. INTRODUCTION

In vivo molecular imaging focuses on the non-invasive detection and characterization of target structures with specific probes (1,2). Based on their unmatched binding specificity and affinity, monoclonal antibodies are considered the most specific probes for targeted imaging (3–5). However, their preclinical and clinical utility is limited due to their relatively poor and slow tissue penetration, slow clearance from circulation, and long retention in non-targeted tissues (6). These characteristics impair their signal-to-background ratio (7). The development of new contrast agents and novel engineered forms of antibodies, such as diabodies, minibodies, single-chain variable fragments, and nanobodies, has triggered a new wave of antibody-based imaging approaches (3,5,6,8). Among these, nanobodies are the smallest available antigen-binding fragments derived from camelid heavy-chain-only antibodies (9,10). With only ~15–18 kDa, these small antibody fragments are soluble, very stable and are renally cleared from the circulation (9,11). These properties make them particularly suited for specific and efficient targeting of tumor antigens *in vivo* (12–20).

* *Correspondence to: Peter Bannas, University Medical Center Hamburg-Eppendorf, Department of Radiology, Martinistrasse 52, 20246 Hamburg, Germany. E-mail: p.bannas@uke.de*

† *These authors contributed equally.*

a *P. Bannas, A. Lenz, V. Kunick, L. Well, W. Fumey, J. Schmid, K. Schütze, G. Adam, H. Ittrich*
Department of Diagnostic and Interventional Radiology, University Medical Center Hamburg-Eppendorf, Hamburg, Germany

b *A. Lenz, V. Kunick, L. Well, W. Fumey, B. Rissiek, F. Haag, J. Schmid, K. Schütze, A. Eichhoff, F. Koch-Nolte*
Institute of Immunology, University Medical Center Hamburg-Eppendorf, Hamburg, Germany

c *B. Rissiek*
Department of Neurology, University Medical Center Hamburg-Eppendorf, Hamburg, Germany

d *M. Trepel*
Department of Oncology and Hematology, University Medical Center Hamburg-Eppendorf, Hamburg, Germany

 Copyright © 2015 John Wiley & Sons, Ltd.

Recent studies have shown that nanobodies allow higher tumor-to-background (T/B) ratios than conventional antibodies in molecular imaging applications *in vivo* (17,19). However, the T/B ratio depends on two parameters: specific binding of the antibody-construct leading to accumulation in the tumor as well as clearance of unbound constructs from the body. Both parameters depend on the molecular size of the probe. A small nanobody (~15 kDa) is expected to penetrate tumor tissue more rapidly than a larger conventional antibody (150 kDa). In turn, clearance of a nanobody via the kidney is fast, leading to short circulation times with a half-life of only ~1.5 h, as compared to days or weeks of conventional antibodies (3,11,21). Therefore, the comparison of two differently sized antibody-constructs for specific imaging of targets *in vivo* has to take into account the different kinetics of tumor accumulation and elimination from the circulation (11). This means that different imaging time points have to be investigated to determine best imaging conditions for each individual antibody construct. Moreover, different doses of the antibodies have to be compared, since higher doses may increase both specific and unspecific signals alike, thus reducing the maximum achievable T/B ratio.

There are only few studies directly comparing nanobodies and conventional antibodies for *in vivo* molecular imaging. Moreover, these studies did not optimize the doses of the conventional antibody and some used high doses of up to 100 μg antibody per animal (17,19). The high dosage inevitably leads to an excess of free circulating antibodies. When assessing T/B ratios based on the region of interest (ROI) in near-infrared fluorescence (NIRF) imaging experiments, the signal of the normal tissue serving as "background" will increase by the circulating antibodies. This results in lower T/B ratios of antibodies compared to nanobodies, not due to differences in specific signal, but due to higher unspecific background signal. Moreover, these excess antibodies are all prone to non-specific accumulation in target antigen-negative tumors by the enhanced permeability and retention (EPR) effect (22,23). Apart from kinetics and dosage, an intraindividual assessment of antigen-positive and -negative xenografts would enable a direct comparison of specific and unspecific signals due to the EPR effect. In addition, a comparative *ex vivo* analysis of explanted tumors would further determine the specificity observed in imaging experiments *in vivo* to optimize imaging conditions of differently sized constructs.

Therefore, we performed a direct NIRF-imaging comparison of a single-domain nanobody (*s+16a*, 17 kDa) and a monoclonal antibody (*Nika102*, 150 kDa) directed to the same target to improve specific *in vivo* NIRF-imaging in a lymphoma xenograft model. S+16 is a nanobody (single variable domain) derived from a heavy-chain-only llama antibody. Nika102 is a conventional monoclonal antibody (rat IgG2a kappa, composed of two heavy chains and two light chains) (Fig. 1A). Compared to mAb Nika102, nanobody s+16a exhibits a lower binding affinity (40 nM vs. 5 nM) and shorter *in vivo* blood half-life (2 h vs. 8 days) (11,24,25). The model target antigen ADP-ribosyltransferase ARTC2 is expressed on the surface of lymphoma cells (25–29). Beyond assessment of the advantages and disadvantages of nanobodies and conventional antibodies, this study was designed to determine the specific requirements, such as timing and dosage, for optimum imaging of tumors.

2. RESULTS

Purity of s+16a and Nika102 before and after conjugation to AF680 was confirmed (Fig. 1B). Assessment of binding affinities showed less than 10% reduction in labeling efficiencies upon overnight incubation in serum (Fig. 1C). Competition studies revealed that nanobody s+16a and antibody Nika102 recognize different epitopes of ARTC2 (Fig. 1D). Internalization studies showed prominent staining of the cell surface upon incubation of cells at 4°C with both constructs. Upon incubation at 37°C, most of the labeled nanobody s+16a^{680} and antibody Nika102^{680} remained on the cell surface. Patchy cytosolic staining with both constructs after incubation for 24 h at 37°C indicates that a fraction of fluorescent label is internalized during prolonged incubation at 37°C (online Supplementary Fig. 1).

2.1. *In vitro* NIRF-imaging experiments

Flow cytometry showed specific labeling of ARTC2-transfected DC27.10 lymphoma cells with s+16a^{680} and Nika102^{680}, but not of parental ARTC2-negative DC27.10 cells (Fig. 2A). Staining with s+16a^{680} yielded lower fluorescence intensities (MFI = 15100 ± 1700) as compared to Nika102^{680} (MFI = 73300 ± 1500), which reflects the lower labeling efficiency with fluorochrome AF680 of s+16a compared to Nika102 (0.3 dyes/molecule for s+16a as compared to 2.0 dyes/molecule for Nika102). To provide a basis for the subsequent *in vivo* and *ex vivo* xenograft experiments, we further analyzed the same cells *in vitro* by fluorescence microscopy and with the NIRF-imaging system. Labeling of s+16a and Nika102 with AF680 not only allowed detection of ARTC2-positive cells with fluorescence microscopy but also semi-quantitative analyses with the NIRF-imaging system intended for *in vivo* experiments (Fig. 2B, C). ARTC2-negative cells showed no detectable signals using either technique. As shown by flow cytometry, the fluorescence signal detected from ARTC2-positive cells with the NIRF-imaging system was lower when labeled with s+16a^{680} (radiant efficiency = $5.1 \pm 2.1 \times 10^7$) than with Nika102^{680} (radiant efficiency = $9.4 \pm 2.5 \times 10^7$). Signals from ARTC2-negative cells were more than 10 times lower than those of ARTC2-positive cells for s+16a^{680} (radiant efficiency = $3.0 \pm 1.5 \times 10^6$) as well as for Nika102^{680} (radiant efficiency = $3.5 \pm 2.3 \times 10^6$).

2.2. NIRF-imaging experiments *in vivo*

Next, we aimed to evaluate the suitability of Alexa-680-conjugated nanobodies and antibodies for *in vivo* imaging of ARTC2-positive tumors. Therefore, we intravenously injected s+16a^{680} and Nika102^{680} into mice at four different doses (5, 10, 25, and 50 μg) 7–9 days after subcutaneous injection of ARTC2-positive and ARTC2-negative DC27.10 lymphoma cells on the opposite flanks of the same animals. The injected doses correspond to 0.004, 0.009, 0.022, and 0.044 mg of dye/kg for s+16a^{680} and to 0.003, 0.006, 0.016, and 0.032 mg of dye/kg for Nika102^{680} for a mouse of 24 g. Imaging was performed before and at defined time-points over 24 h after injection of the fluorochrome conjugates (Figs. 3 and 4 and Supplementary Fig. 1). The results showed efficient and specific labeling of ARTC2-positive tumors with both constructs. When injected with Nika102^{680}, the specific signal in ARTC2-expressing tumors slowly increased over time, whereas after injection of s+16a^{680}, the signal was already strong at early time points and declined over time (Fig. 3). Both constructs showed higher signals of ARTC2-positive tumors with increasing concentrations. At early time points after injection of s+16a^{680}, strong signals were observed also in the kidneys, reflecting passage of the nanobodies through the renal filtration barrier. Note the high background signals of the entire animal

Copyright © 2015 John Wiley & Sons, Ltd.

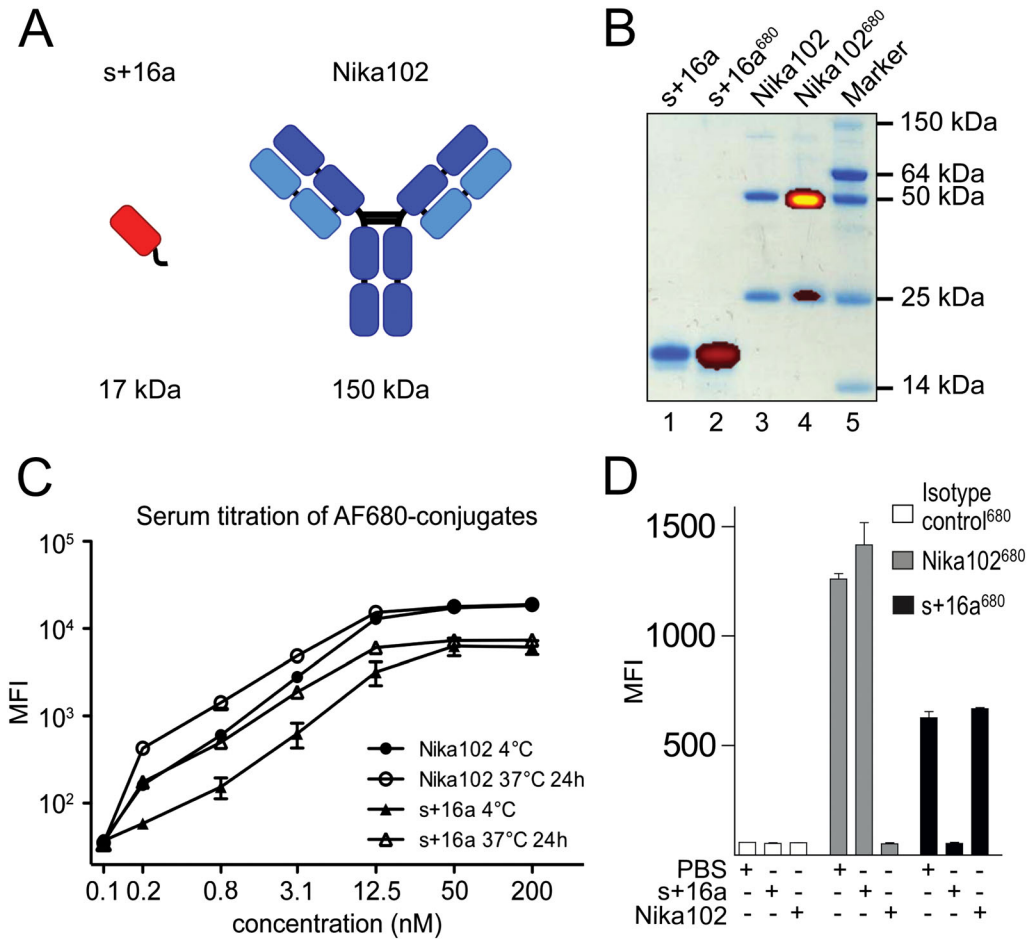

Figure 1. Structure, purity, stability and competition study of ARTC2-specific AF680-conjugates. (A) Scheme of nanobody s+16a and mAb Nika102. (B) Coomassie-stained gel overlaid by a corresponding NIRF image of unconjugated s+16a and Nika102 (lanes 1 and 3) and respective AF680-conjugates (lanes 2 and 4) (1 μg per lane of any given conjugate). (C) To asses the stability of the AF680-conjugates, conjugates were serially diluted and incubated for 24 h either at 4°C in PBS or at 37°C in serum. Conjugates were then used to stain ARTC2-expressing lymphoma cells before analysis by flow cytometry. Fluorescence intensities of the mean ± SD from three independent experiments are plotted. (D) ARTC2-expressing lymphoma cells were pretreated with PBS, unlabeled s+16a or Nika102 before staining with fluorochrome-conjugated Nika102, s+16a or isotype control antibodies and analysis by flow cytometry.

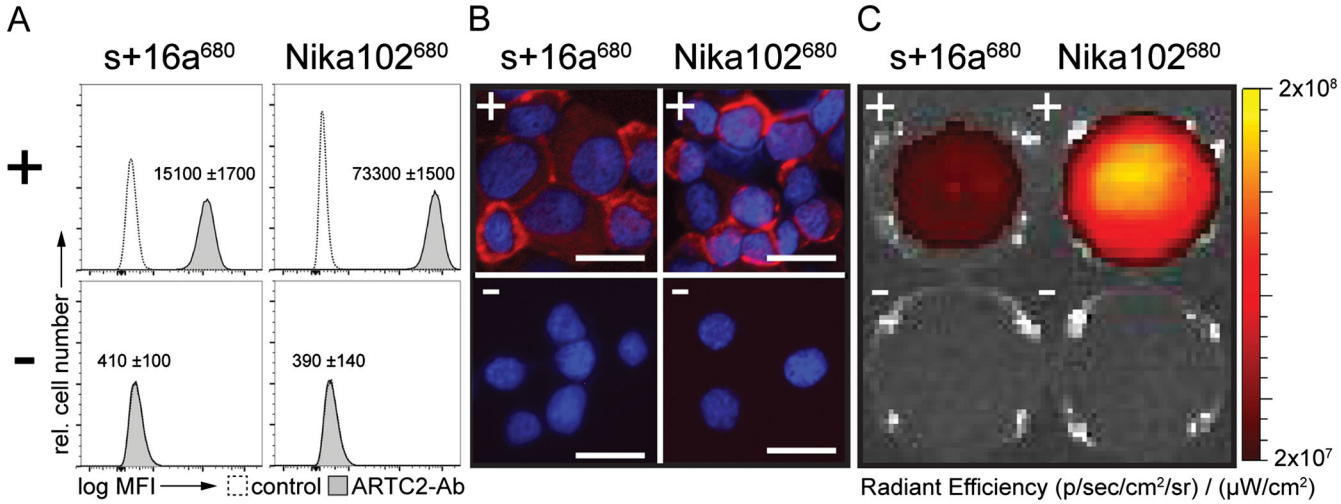

Figure 2. Imaging of AF680-conjugates *in vitro*. Untransfected (−) and ARTC2-transfected (+) DC27.10 lymphoma cells were incubated with s+16a^{680} and Nika102^{680}. (A) One aliquot of labeled cells (1×10^6) was subjected to flow cytometry to quantify cell-bound AF680 conjugates. Mean fluorescence intensity of ARTC2 expression on lymphoma cells is plotted. Numbers indicate mean ± SD fluorescence intensity of ARTC2-positive cells (grey histograms) from three independent experiments. Unfilled histograms show isotype controls. (B) Another aliquot of labeled cells (1×10^5) was used for fluorescence microscopic analysis of specific ARTC2 labeling (red). Nuclei were counter-stained with DAPI (blue). The size bar indicates 10 μm. (C) A third aliquot of cells (1×10^7) was transferred onto a 96-well plate for NIRF imaging *in vitro*. Results are representative of three independent experiments.

 Copyright © 2015 John Wiley & Sons, Ltd.

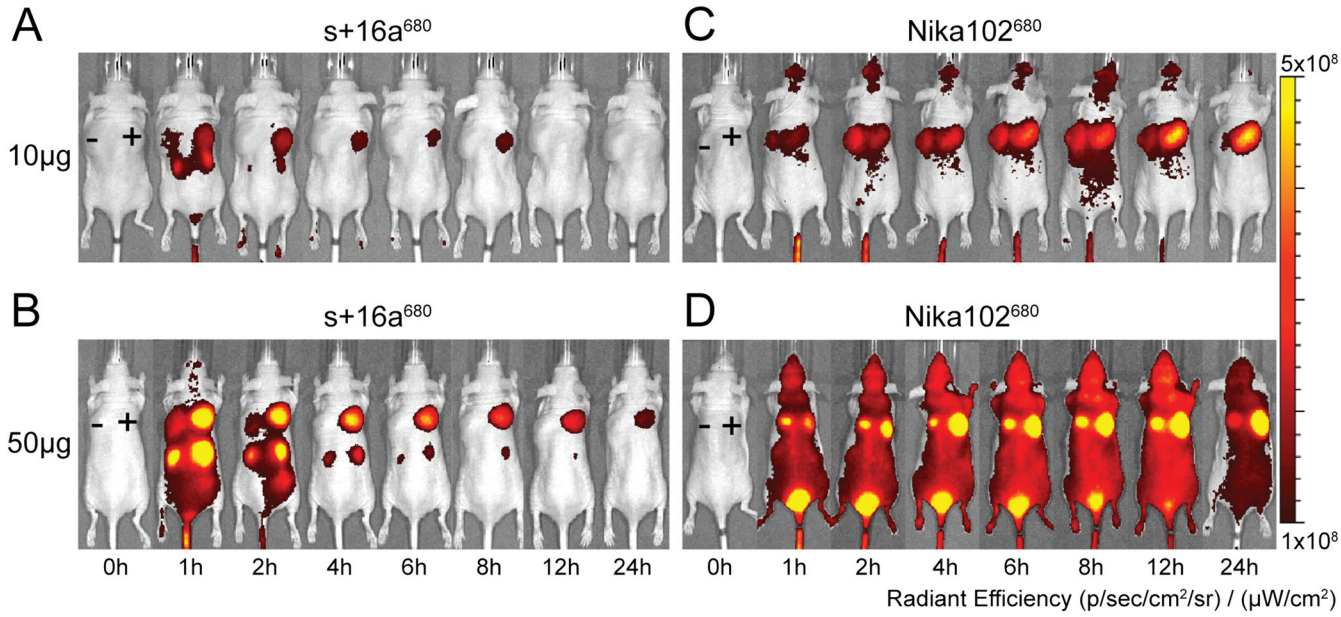

Figure 3. Comparison of different doses and time points for specific NIRF imaging *in vivo*. Seven to nine days after subcutaneous implantation of ARTC2-positive (+) and ARTC2-negative (-) lymphomas, s+16a^{680} (A, B) and Nika102^{680} (C, D) were injected intravenously at a dose of 10 µg (A, C) or 50 µg (B, D), respectively. NIRF imaging was performed before and 1, 2, 4, 6, 8, 12, and 24 h after injection. Signal intensities of all injected mice and imaging time points are all equally leveled to allow direct and fair visual comparison. Results are representative of at least three independent experiments. Levels of statistical significance are indicated by asterisks (* = $p < 0.05$, ** = $p < 0.01$, *** = $p < 0.001$).

after injection of 50 µg of Nika102^{680} and the unspecific signals of the negative tumor when using higher doses of Nika102^{680} (Figs. 3D and 4A).

The intermediate dose of 25 µg showed lower specific signals for both s+16a^{680} and Nika102^{680} as compared to 50 µg and higher specific signals as compared to 10 µg (Supplementary Fig. 2). The dose of 25 µg also showed higher unspecific signals in ART2-negative tumors for Nika102^{680} resulting in a lower T/B-ratio as compared to 10 µg. The lowest dose of 5 µg showed the lowest specific and unspecific signals for both constructs with lowest resulting T/B ratios. In summary, the comparison of different doses of AF680-conjugates showed best imaging results with 50 µg of s+16a^{680} and with 10 µg of Nika102^{680} by achieving highest specific signal intensities (s+16a^{680}) and by minimizing unspecific signals of ARTC2-negative tumors and background while maintaining sufficient specific signals (Nika102^{680}), thereby allowing for highest T/B-ratios.

Semi-quantitative ROI analyses confirmed a rapidly increasing T/B ratio of ARTC2-positive tumors after injection of s+16a^{680}, which reached a maximum of 12.4 ± 4.2 (50 µg) and 4.7 ± 0.1 (10 µg), respectively, already 4–6 h post-injection (Fig. 4B). The T/B ratio of ARTC2-positive tumors detected with s+16a^{680} was significantly higher than of ARTC2-negative tumors throughout 2 h to 24 h post-injection. In contrast, the T/B ratio using Nika102^{680} increased only slowly and reached its maximum of 8.7 ± 3.9 (10 µg) and 6.1 ± 2.0 (50 µg), respectively, not until 24 h post-injection. In the case of Nika102^{680}, the T/B ratio of ARTC2-positive tumors was not significantly higher than of ARTC2-negative tumors until 8 h to 24 h post-injection due to the high unspecific signal of ARTC2-negative tumors.

The need to evaluate different time points and different doses when comparing differently sized antibodies for coherent NIRF-imaging experiments is illustrated in Fig. 5. The direct comparison of the T/B ratios obtained by using either 10 µg or 50 µg of each AF680-conjugate at different time points revealed that in the case of s+16a^{680}, significantly higher T/B ratios can be obtained with the higher concentration of 50 µg 4 to 6 h post-injection. Interestingly, in Nika102^{680}-injected mice, a significant difference between the two dosing regimens was seen only after 24 h, and, as shown above, with a higher T/B ratio obtained by the lower concentration of 10 µg Nika102^{680}. Based upon these observations, the following *ex vivo* experiments were performed at the optimum imaging time points and optimum probe concentrations of 6 h and 50 µg for s+16a^{680} and of 24 h and 10 µg for Nika102^{680}.

2.3. NIRF-imaging experiments *ex vivo*

ARTC2-positive and ARTC2-negative tumors were explanted 6 h and 24 h post-injection to quantify tumor-associated fluorescence and T/B ratios in the absence of potentially confounding signals from other tissues. The results of NIRF-imaging *ex vivo* reflect those of the *in vivo* experiments (Fig. 6). Both AF680 conjugates showed high signals from ARTC2-positive tumors, which decreased for s+16a^{680} and increased for Nika102^{680} over time (Fig. 6A). Signals of ARTC2-positive tumors were significantly higher than of ARTC2-negative tumors in the case of s+16a^{680} only at 6 h ($p < 0.001$) and in the case of Nika102^{680} only at 24 h ($p < 0.05$) post-injection. Note the low unspecific signal of ARTC2-negative tumors after injection of s+16a^{680} at both time points, as compared to the high unspecific signal of ARTC2-negative tumors after injection of Nika102^{680}. In the case of s+16a^{680}, the T/B ratio of dissected ARTC2-positive tumors was significantly higher than that of ARTC2-negative tumors at both time points, 6 h and 24 h post injection ($p < 0.01$ and $p < 0.05$, respectively) (Fig. 6B). As for the absolute signal intensities, Nika102^{680} culminated in a significantly higher T/B ratio of positive tumors as compared to negative tumors only 24 h post-injection ($p < 0.05$). Note the much higher T/B ratio (61.4 ± 30.9) of ARTC2-positive tumors 24 h post-injection of Nika102^{680} as compared to the maximum achievable T/B ratio of s+16a^{680}

Copyright © 2015 John Wiley & Sons, Ltd.

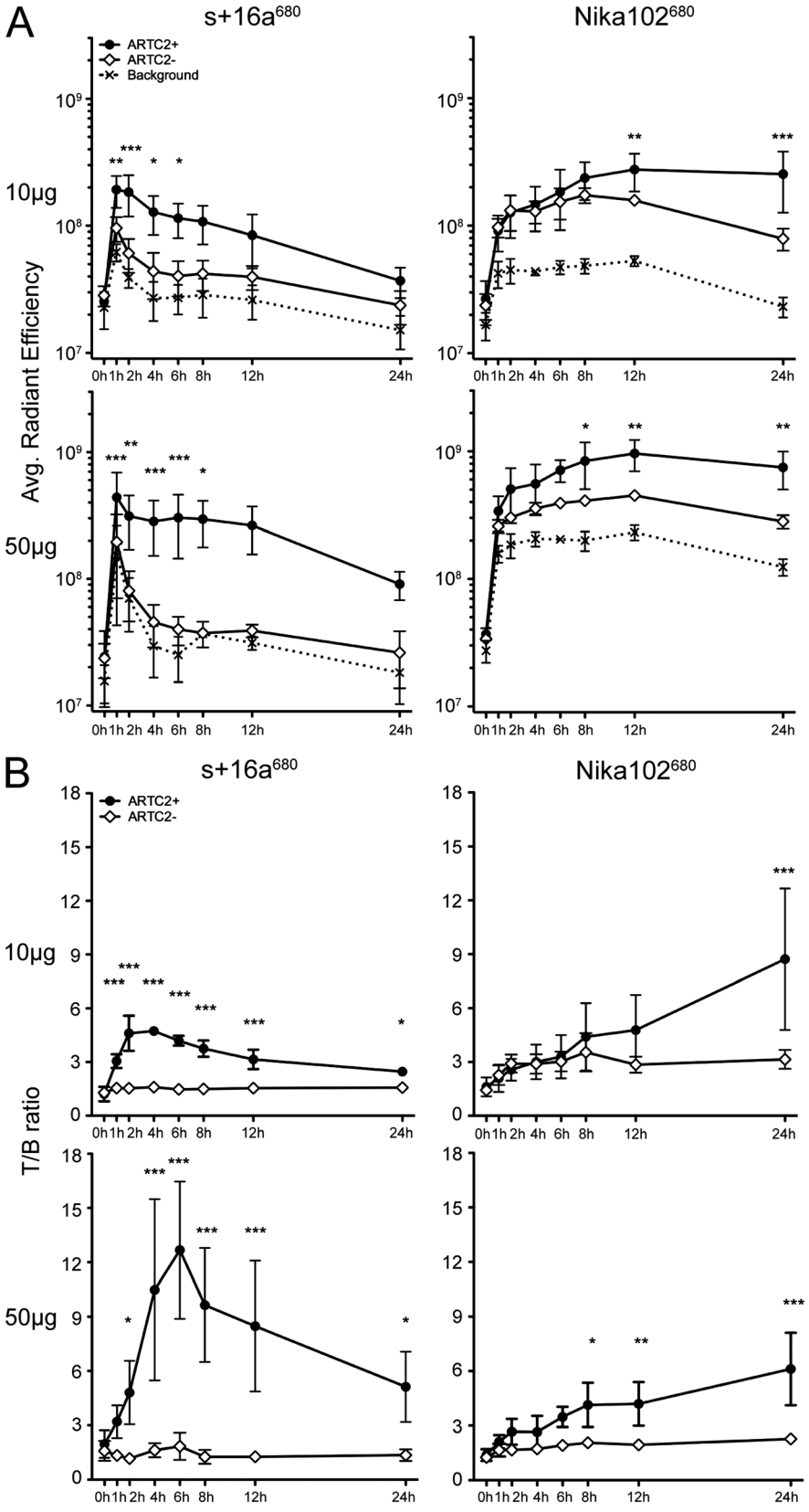

Figure 4. Radiant efficiency and T/B ratio of ARTC2-positive and ARTC2-negative tumors *in vivo*. S+16a^{680} and Nika102^{680} were injected into ARTC2-positive and ARTC2-negative tumor-bearing mice at a dose of 10 µg (upper panels) or 50 µg (lower panels), respectively. NIRF imaging was performed at different time points after injection and ROIs were drawn around tumors and normal tissue (hind leg) for semi-quantitative analyses. (A) Radiant efficiencies and (B) calculated T/B ratios of ARTC2-positive and ARTC2-negative tumors as well as background signals are plotted as a function of time. Data are presented as mean ± SD from at least three independent experiments for each group. Levels of statistical significance are indicated by asterisks (* = $p < 0.05$, ** = $p < 0.01$, *** = $p < 0.001$).

Copyright © 2015 John Wiley & Sons, Ltd.

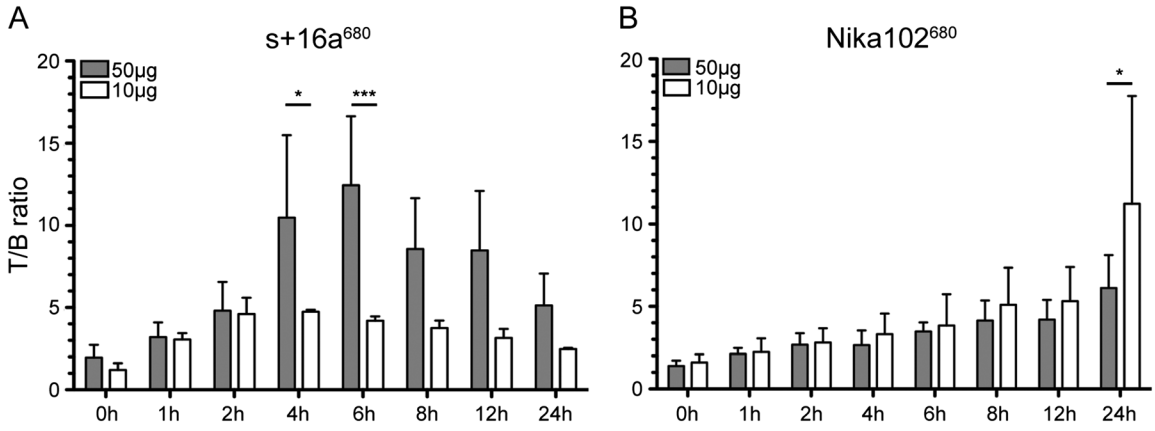

Figure 5. Optimization of probe concentration and NIRF-imaging time point for maximal T/B ratio of s+16a^{680} and Nika102^{680} *in vivo*. T/B ratios obtained from NIRF imaging of ARTC2-positive tumors are plotted as a function of time for mice injected with either 10 µg (white columns) or 50 µg (grey columns) of (A) s+16a^{680} and (B) Nika102^{680}, respectively. Fifty micrograms of s+16a^{680} showed a higher T/B ratio than 10 µg, which was significant 4–6 h post-injection. Nika102^{680} showed the opposite behavior, the lower dose yielded a higher T/B ratio than the higher dose, which became significant after 24 h. Data are presented as mean ± SD from three to seven independent experiments. Levels of statistical significance are indicated by asterisks (ns = $p > 0.05$, * = $p < 0.05$, ** = $p < 0.01$, *** = $p < 0.001$).

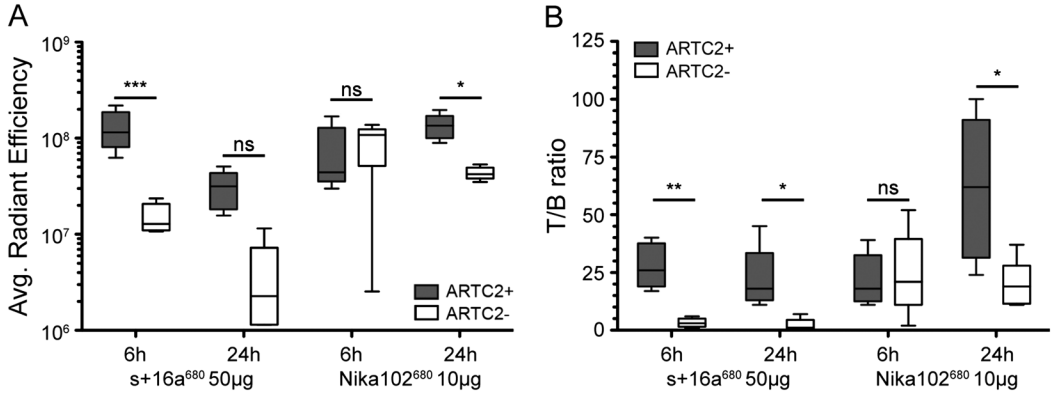

Figure 6. NIRF imaging *ex vivo*. ARTC2-positive (+) and ARTC2-negative (−) tumors of mice injected with 50 µg s+16a^{680} or with 10 µg Nika102^{680} were explanted 6 h and 24 h post-injection in order to quantitate tumor-associated fluorescence and T/B ratios using NIRF imaging in the absence of potentially confounding signals from other tissues. (A) Radiant efficiencies of tumors and (B) T/B ratios are presented as mean ± SD from five independent experiments.

(27.8 ± 9.6) after 6 h in the absence of confounding signals from normal tissue.

Biodistribution analyses of spleen, lungs, liver, kidneys, stomach, ileum, and muscle revealed an overall decline of signal intensities at 24 h as compared to 6 h (Fig. 7A). At both time points, 6 h and 24 h post-injection, the highest unspecific organ-to-background ratios were observed for the liver in the case of Nika102^{680} and for the kidneys in the case of s+16a^{680} (Fig. 7B). Interestingly, in the case of Nika102^{680}, at 6 h post-injection the second highest organ-to-background ratio was observed for the ARTC2-negative tumor and at 24 h the ARTC2-negative tumor showed even the highest unspecific signals when compared to other organs.

2.4. Flow cytometry and fluorescence microscopy *ex vivo*

Next, we determined possible causes of the unspecific signals from normal tissue after injection of Nika102^{680} *in vivo* (Figs. 3D, 4A) as well as from ARTC2-negative tumors *in vivo* and *ex vivo* (Figs. 4A and 6). Therefore, we performed flow cytometry *ex vivo* to quantify levels of unbound AF680-conjugates in serum and of cell bound AF680-conjugates on dispersed cells from the explanted tumors (Fig. 8). Serum samples showed little, if any, detectable circulating s+16a^{680} at 6 h and 24 h post-injection (Fig. 8A). In contrast, mice that had been injected with Nika102^{680} showed significantly higher levels of unbound circulating Nika102^{680} in serum at both time points, which somewhat decreased over time, but were still present in excess 24 h post-injection. Urine analyses revealed high levels of s+16a^{680}, particularly 6 h post-injection, but little, if any, Nika102^{680} (data not shown).

Flow cytometry of dispersed cells from xenografts dissected 6 h and 24 h post-injection showed specific labeling of ARTC2-positive lymphoma cells with both AF680-conjugates and no unspecific labeling of ARTC2-negative tumor cells (Fig. 8B). As seen with NIRF-imaging *in vivo* and *ex vivo*, labeling and specific signals from ARTC2-positive tumors decreased over time after injection of s+16a^{680}, whereas signals of ARTC2-positive tumors from animals injected with Nika102^{680} increased over time. Signals of cells from ARTC2-positive tumors from animals injected with s+16a^{680} were higher than signals after injection of Nika102^{680} at 6 h post injection, but lower at 24 h after injection.

Copyright © 2015 John Wiley & Sons, Ltd.

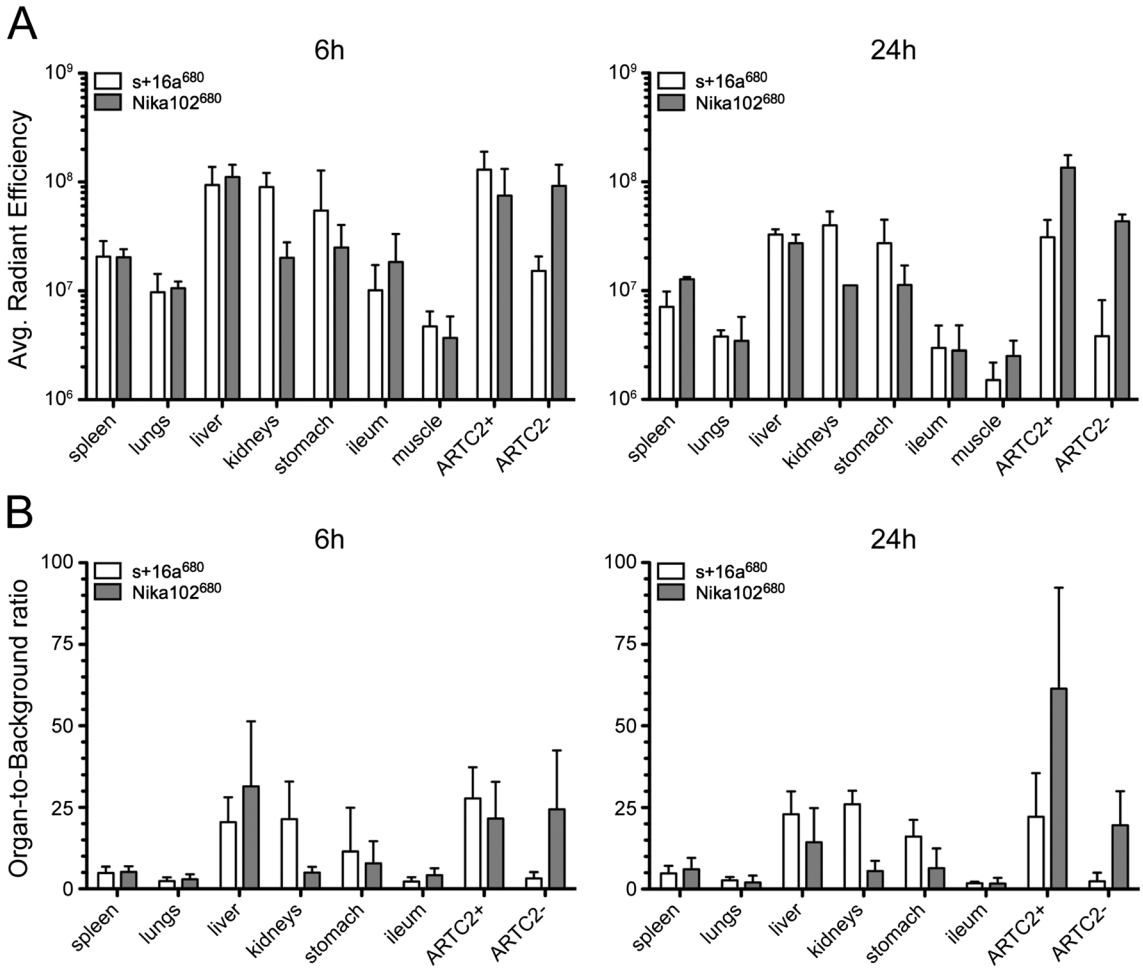

Figure 7. Biodistribution analyses. At 6 h and 24 h post-injection of 50 μg s+16a^{680} or 10 μg Nika102^{680} mice were sacrificed and tumors and organs were explanted. (A) Organ- and tumor-associated fluorescence was quantified and (B) organ- and tumor-to-background ratios were calculated using NIRF imaging in the absence of confounding signals from other tissues. Signals from explanted muscle tissue served as background value to calculate ratios. Radiant efficiencies of organs and tumors and organ- and tumor-to-background ratios are presented as mean ± SD from five independent experiments.

We further analyzed the distribution of injected AF680-conjugates within explanted and cryosectioned tumors *ex vivo* by confocal fluorescence microscopy (Fig. 9). S+16a^{680} revealed homogeneous and specific labeling of ARTC2-positive tumor cells 6 h post-injection, similar to the staining of these cells in culture (Fig. 2B). In contrast, Nika102^{680} showed only weak staining of cells in ARTC2-positive tumors after 6 h. Moreover, the monoclonal antibody showed staining evidently not associated with tumor cells in both ARTC2-positive and ARTC2-negative tumors (Fig. 9A, arrow).

3. DISCUSSION

The utility for both nanobodies and conventional antibodies for *in vivo* imaging is well established, but optimum dosing and timing schedules for one versus the other have not been determined so far. Here, we used NIRF-dye AF680-conjugated nanobodies and conventional monoclonal antibodies directed at the same target on lymphoma cells for a direct comparison of *in vivo* and *ex vivo* analyses. We showed that nanobodies are well suited as diagnostic tools for rapid and specific *in vivo* detection of lymphomas, with superior tissue penetration compared to conventional antibodies and significantly higher T/B ratios when performing same-day imaging *in vivo*. In addition, our experiments revealed that at later time points the T/B ratio of conventional antibodies can be improved by using lower doses of antibody conjugates.

In vitro, both, nanobody s+16a^{680} and antibody Nika102^{680} bound specifically to ARTC2-positive lymphoma cells with no unspecific labeling of ARTC2-negative cells (Fig. 2). Albeit that Nika102^{680} showed stronger signals *in vitro*, s+16a^{680} allowed a faster and more specific detection of ARTC2-positive xenografts *in vivo* (Figs. 3 and 4). Apart from the different kinetics for best tumor visualization *in vivo*, the major drawback of Nika102^{680} at higher doses (50 μg) was the high unspecific signal originating not only from normal tissues (causing fluorescence signals from the entire mouse), but also from ARTC2-negative tumors (Fig. 4). This apparently insufficient T/B ratio could be improved by using a lower dose (10 μg) of Nika102^{680}, resulting in dramatically reduced signals of normal tissues and ARTC2-negative tumors and only slightly decreased specific signals of ARTC2-positive tumors (Fig. 5). In contrast, increasing the dose of s+16a^{680} caused stronger signals of ARTC2-positive tumors but not of normal tissue or ARTC2-negative tumors.

NIRF imaging of dissected tumors *ex vivo* revealed the overall strongest T/B ratio of ARTC2-positive tumors 24 h post-injection

Copyright © 2015 John Wiley & Sons, Ltd.

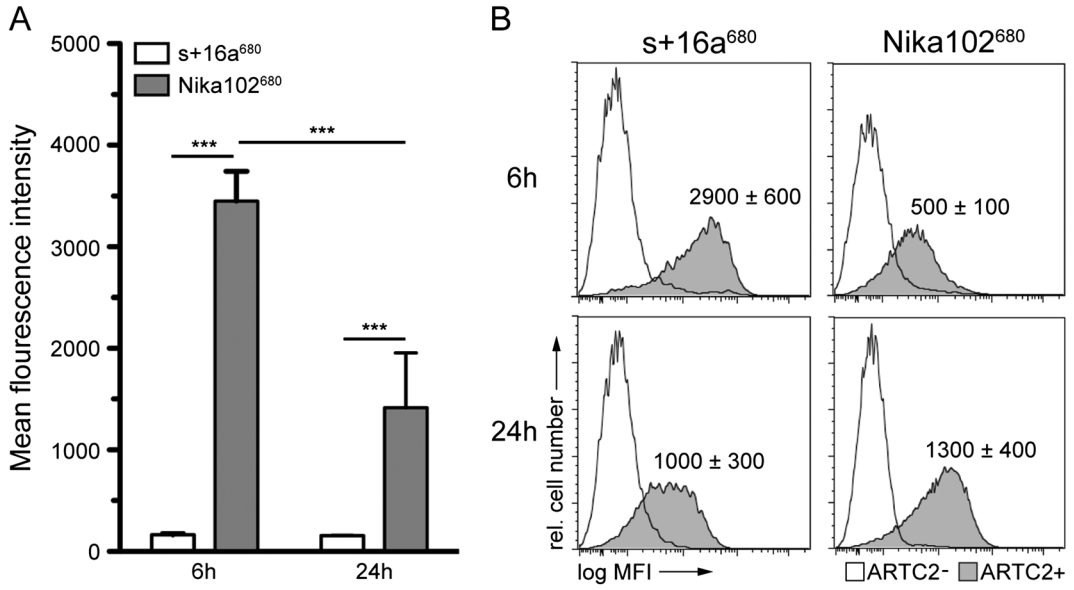

Figure 8. Flow cytometric analyses of circulating and cell bound s+16a^{680} and Nika102^{680}. (A) In order to determine a cause for the high background signals and the unspecific signal of ARTC2-negative tumors post-injection of Nika102^{680}, we analyzed serum to monitor levels of circulating unbound AF680-conjugates. Mice bearing ARTC2-negative and ARTC2-positive tumors were injected intravenously with 50 μg s+16a^{680} and 10 μg Nika102^{680} and sacrificed 6 h and 24 h after injection. Serum at a dilution of 1:100 was used to label ARTC2-transfected lymphoma cells for flow cytometric quantification of circulating intact AF680 conjugates. Fluorescence intensities of the mean ± SD from three independent experiments are plotted. Levels of statistical significance are indicated by asterisks (*** = $p < 0.001$). (B) To determine the level of injected conjugates specifically bound to tumor cells both ARTC2-positive and ARTC2-negative tumors were dissected from the same animals. Single-cell suspensions were counterstained with anti-CD45 and analyzed by flow cytometry to quantify the amount of cell-bound AF680 conjugates. Means and standard deviations of fluorescence intensities (MFI) from three independent experiments are plotted.

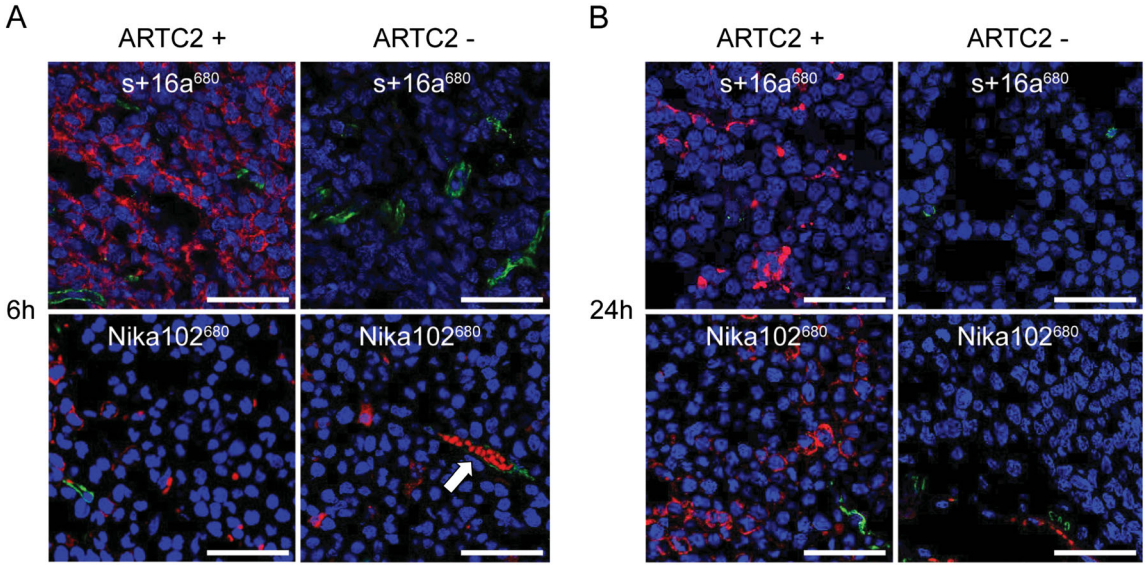

Figure 9. Fluorescence microscopy *ex vivo* of ARTC2-positive and ARTC2-negative tumors. Confocal fluorescence microscopy (40×) of tumor cryosections (A) 6 h and (B) 24 h post-injection of 50 μg s+16a^{680} and 10 μg Nika102^{680}, respectively. Signal intensities of AF680-conjugates are displayed in red and demonstrate the distribution within the tumor 6 h and 24 h after injection. Nuclei were counter-stained *ex vivo* with DAPI (blue) and blood vessels were stained with anti-CD31^{488} (green). Nanobody s+16a^{680} revealed homogeneous and specific labeling of ARTC2-positive tumors readily within 6 h, whereas Nika102^{680} showed weak staining after 6 h, which increased only after 24 h. At both imaging time points Nika102^{680} also showed unspecific staining within or close to the tumor vasculature (arrow) of both ARTC2-negative and positive tumors. The size bar indicates 50 μm. These results are representative of three independent experiments.

of Nika102^{680} in the absence of potentially confounding signals from other tissues (Fig. 5). These *in vivo* and *ex vivo* NIRF-imaging observations could be well explained by the results of *ex vivo* flow cytometric analyses for quantification of injected AF680-conjugates in serum (Fig. 8A). These showed high levels of unbound and free circulating Nika102^{680} 6 h and even 24 h post-injection, even at the lower dose of 10 μg, whereas after the injection of 50 μg of s+16a^{680} no unbound nanobodies were

Copyright © 2015 John Wiley & Sons, Ltd.

detectable in serum at these time points. These results are in accordance with a recent study in which we determined the pharmacokinetics of s+16a^{680} and Nika102^{680} (11). It is conceivable, that higher doses would further increase the amount of free circulating Nika102^{680}, and thereby further increase the observed unspecific signals *in vivo*. *Ex vivo* flow cytometric analyses of dispersed cells from dissected tumors showed specific staining of ARTC2-positive tumor cells with both constructs but no unspecific binding of injected AF680-conjugates to ARTC2-negative lymphoma cells (Fig. 8B). These findings are consistent with *in vitro* labeling experiments, which show prominent cell-surface staining of ART2-positive tumor cells as well as some internalized fluorescence for both constructs after 24 h incubation at 37°C (Supplementary Fig. 1). The higher staining intensity of ART2-positive tumor cells with nanobody s+16a^{680} than with mAb Nika102^{680} at 6 h post-injection likely reflects the higher injected dose and faster tissue penetration of the nanobody. The lower staining intensity of ART2-positive tumor cells with nanobody s+16a^{680} than with mAb Nika102^{680} at 24 h post-injection likely reflects the lower affinity and renal elimination of excess nanobody. The increase in staining intensity of mAb Nika102^{680} at 24 h versus 6 h likely reflects increasing accumulation in the tumor from excess levels of circulating mAb. Fluorescence microscopy completed the *ex vivo* imaging approach. In the case of the nanobody s+16a, homogeneous staining of cells in ART2C-positive tumor sections correlated well with the staining of cells *in vitro* (Figs. 9A and 2B), confirming that the nanobody was able to reach even remote areas within the tumor after 6 h. In contrast, the monoclonal antibody showed only weak staining of cells in ARTC2-positive tumors after 6 h. Moreover, the monoclonal antibody showed staining within or close to the tumor vasculature even in ARTC2-negative tumors (Fig. 9A), providing a plausible explanation for the unspecific signals during *in vivo* imaging. The better tissue penetration of the nanobody s+16a at early time points is likely attributed to its ability to cross the endothelial barrier more easily to reach its target.

NIRF imaging of other organs *ex vivo* revealed high unspecific signals for the liver in the case of Nika102^{680} and for kidneys in the case of s+16a^{680}. High signals in the kidney at early time points are consistent with renal filtration and partial retention of nanobody s+16a^{680} in the kidneys. High signals in the liver for both constructs are consistent with hepatic elimination of fluorochromes. Note that at the time point of *ex vivo* analyses (6 h and 24 h), the signals from kidneys had already decreased dramatically as compared to the *in vivo* signals at 1 h and 2 h post-injection, presumably by elimination of most of labeled nanobody s+16a^{680} from the body via urination. Signals from the kidneys even after 24 h likely reflect partial tubular resorption of nanobodies and/or fluorochromes.

As in previous studies, the results reported here emphasize that molecular imaging with labeled nanobodies *in vivo* allows rapid and specific same-day tumor imaging, including the possibility of increasing the dose for optimized T/B ratios without compromising specificity of marked tissues (12–15,17–19). Our study also reveals, that *in vivo* molecular imaging using conventional antibodies can be considerably improved by determining the optimum dose of the injected large (and therefore not renally cleared) antibodies. A fivefold lower dose of conventional antibody can almost double the T/B ratio. Recent studies, comparing nanobodies and conventional antibodies for *in vivo* molecular imaging neglected to optimize the dose of the investigated conventional antibody and used very high doses of up to 100 μg per animal (17,19). This leads to an excess of free-circulating antibodies, as we were able to show for mAb Nika102^{680} in the present study. These excess antibodies are prone to nonspecific accumulation in target-negative tumors by the enhanced permeability and retention effect (EPR) described earlier for conventional antibodies (22,23). It should be noted, that the EPR effect also leads to an increased uptake of antibodies in the target-positive tumors and may thereby contribute to increase the specific signals at low antibody doses. Taken together, thorough dose optimization of conventional antibodies should be performed for *in vivo* imaging applications.

For nanobodies, in contrast, dose optimization seems to be less of an issue, since any excess is renally cleared within 2 h and thus unspecific accumulation in non-targeted tissue is minimized. This allows same-day imaging and could be translatable to the clinical setting. However, next-day imaging might be more convenient in a clinical setting. Further, the cost efficiency might be better for the antibody due to the lower dose required, even though nanobodies can be produced at low costs in bacteria and yeast (10).

A limitation of our study is that we did not optimize the amount of fluorescent dyes per antibody construct, which might affect the maximum achievable signal for imaging. Another improvement of the labeling strategy would have been the site-specific conjugation of the NIRF dye, as recently described by Kijanka *et al*., instead of random conjugation to primary amine groups, which might affect binding affinity (17). Another limitation is that we injected fixed doses of 5, 10, 25 and 50 μg of our constructs regardless of the weight of the animals, instead of performing weight-adapted injections. The differences in weight of individual mice (range 22.5–26.1 g) may explain some of the observed signal variations within different dose groups.

The region chosen for "background" signal estimation also influences the calculated T/B ratios. However, nanobody s+16a and mAb Nika102 show different accumulations in different abdominal organs and blood, precluding a fair and comparable estimation of T/B ratios with these tissues. As an alternative, we chose the hind limb and muscle, respectively, because this tissue introduced less variation, even though it might underestimate the systemic background.

In addition, further studies should investigate time points later than 24 h post-injection (e.g. 48 h, 72 h). These might show a further improvement of the maximum achievable T/B ratio using the conventional antibody, as recently shown for Trastuzumab by Kijanka *et al*. (17). A limitation of nanobodies in imaging is the high confounding signal of the kidneys due to their renal elimination, which is particularly prominent at early time points. This confounding signal might limit the ability of nanobodies to detect tumors located close to the kidneys. However, the renal retention of nanobodies can be reduced by 45% upon co-injection of gelofusine and lysine without reduced tumor uptake, as reported by Gainkam *et al*. (30).

An intrinsic limitation when comparing llama-derived nanobodies and conventional antibodies is the fact that they bind to different epitopes of the target antigen, which might influence antibody internalization, unspecific binding to other sites or uptake by the reticular endothelial system, thereby affecting blood half-life. However, the differences observed here in terms of dose and timing for optimal imaging can be mainly explained by the size difference of the nanobody and the conventional antibody.

Copyright © 2015 John Wiley & Sons, Ltd.

An inherent technical limitation of NIRF imaging is its low penetration depth of 7–10 mm, which is particularly suited for imaging of subcutaneous tumors but does not allow for imaging of orthotopic tumors. However, even for subcutaneous tumors, some spillover from abdominal organs such as kidneys or liver cannot be excluded. Therefore, thorough *ex vivo* validation experiments of explanted tumors and organs are mandatory. Another limitation of NIRF imaging is the only semi-quantitative assessment of biodistribution as compared to radionuclide-mediated imaging. However, this limitation is compensated in part by the suitability of NIRF-labeled probes for *ex vivo* validation experiments, that is, quantitative flow cytometric assessment of antibodies bound to tumor cells. Moreover, for the principle aim of this study, that is, optimizing timing and dosing of nanobodies and antibodies for imaging *in vivo*, the NIRF technique is well suited. Our results are in accord with a recent study by Oliveira *et al*. using NIRF-labeled nanobodies (19). If desired, nanobodies can also be radiolabeled for positron emission tomography (PET) imaging of xenograft models. A recent study that compared nanobodies and conventional antibodies for PET imaging also came to the conclusion that nanobodies allow same-day imaging with high tumor-to-background ratios (15).

4. CONCLUSIONS

Labeling of nanobody s+16a and antibody Nika102 with AF680 allowed validation of *in vivo* NIRF-imaging results with *ex vivo* flow-cytometry and fluorescence-microscopy. For this reason, and because it is nonradioactive, highly sensitive, inexpensive, and uses comparatively easy-to-produce targeted probes, we advocate the use of the NIRF-imaging technique for evaluation of new antibody constructs in preclinical molecular imaging experiments.

Our comparative *in vivo* and *ex vivo* analyses revealed that the specific contrast between tumor and normal tissue is more important than the absolute amount of conjugate that reaches the tumor. Moreover, our study confirmed that timing and dosage significantly influence specific and unspecific *in vivo* NIRF-imaging signals of s+16a^{680} and Nika102^{680}. Nanobody s+16a allowed same-day imaging with high tumor-to-background ratio, whereas antibody Nika102 gave optimal imaging results only 24 h post-injection. Nanobody s+16 required a high dose while antibody Nika102 had the best tumor-to-background ratio at a low dose. Therefore, timing and dosage should be addressed when using nanobodies and conventional antibodies for molecular imaging purposes.

5. EXPERIMENTAL

5.1. Cell lines and mice

ARTC2-transfected and untransfected DC27.10 murine lymphoma cells were cultured as described previously (26). The closely related ARTC2.1 and ARTC2.2 T cell GPI-anchored cell surface ecto-enzymes are encoded by tandem genes. The study was performed with reagents specific for ARTC2.2, for better legibility we use the term ARTC2. Tumor xenograft experiments were conducted using athymic nude mice (NMRI-*Foxn1*^{nu}) weighting 24.0 ± 1.4 g (range 22.5 to 26.1 g). Mice were obtained from Charles River Laboratories (Sulzfeld, Germany). Experiments were performed in accordance with international guidelines on the ethical use of animals and were approved by the local animal welfare commission.

5.2. Generation of AF680-conjugates

Generation and purification of ARTC2.2-specific nanobody *s+16a* (~17 kDa) and of monoclonal antibody *Nika102* (150 kDa) were described previously (24,25). S+16a carries C-terminal His6x and c-Myc epitope tags and has a calculated size of 17.4 kDa (25). Nanobody s+16a and antibody Nika102 were conjugated to the fluorescent dye AlexaFluor-680 (AF680) (Molecular Probes, Carlsbad, CA, USA) (excitation wavelength = 679 nm, emission wavelength = 702 nm) and number of dye molecules per probe were calculated using molar extinction coefficients of 15720 $cm^{-1} M^{-1}$ and 203000 $cm^{-1} M^{-1}$, respectively. Purity of antibody constructs before and after conjugation to AF680 was assessed by SDS-PAGE size fractionation and Coomassie brilliant blue gel stain as described previously (11). Binding affinities as well as stability during overnight incubation at 37°C in serum were assessed by serial dilution of probes and flow cytometric analyses of labeled DC27.10 cells. Competition studies were performed to evaluate whether s+16a and Nika102 recognize distinct or overlapping epitopes. ARTC2-transfected DC27.10 cells were pretreated with phosphate buffered saline (PBS), unlabeled s+16a (5 μg/100 μL) or unlabeled Nika102 (5 μg/100 μL) for 20 min at 4°C before exposure to AF680-conjugated Nika102 (0.2 μg/100 μL), s+16a (0.2 μg/100 μL) or isotype control antibodies for 20 min and analysed by flow cytometry. Internalization studies were performed by staining of DC27.10 ARTC2 cells with s+16a^{680} Nika102^{680} for 30 min on ice and washed. Cells were further incubated in cell culture medium at 4°C for 2 h or at 37°C for 2 and 24 h before fixation in 2% PFA, counterstaining with Hoechst 33428, and analysis by fluorescence microscopy.

5.3. *In vitro* analyses

For *in vitro* flow-cytometric analyses, 1×10^6 untransfected or ARTC2-transfected DC27.10 cells were stained with s+16a^{680} or Nika102^{680} (1 μg/μL) or control antibodies for 30 min at 4°C. Cells were washed twice and analyzed by flow cytometry on a FACS Canto II (BD Biosciences, Becton Dickinson, Franklin Lakes, USA). Dead cells were excluded after staining with propidium iodide. Flow cytometry data was analyzed with FlowJo 9.3 software (Tree Star Inc, Ashland, OR, USA).

For *in vitro* fluorescence microscopy, 1×10^5 untransfected or ARTC2-transfected DC27.10 cells were stained with either s+16a^{680}, Nika102^{680} or control antibodies as described above. Cells were suspended in a volume of 0.2 mL of PBS and centrifuged (CytoSpin, Shandon, Pittsburgh, PA, USA) onto microscope slides at 800 rpm for 5 min. Cells were fixed in acetone for 10 min, washed twice in PBS, and mounted with Mowiol-DAPI (Molecular Probes, Carlsbad, CA, USA). After air-drying for 24 h, slides were analysed with an inverted microscope (Axiovert 200 m, Zeiss, Goettingen, Germany) with excitation of 665 nm and emission of 725 nm. Images were analyzed with ImageJ software (NIH, Bethesda, Maryland, USA).

For NIRF imaging *in vitro*, 1×10^7 untransfected or ARTC2-transfected DC27.10 cells were stained with either, s+16a^{680}, Nika102^{680} or control antibodies as described above. Cells were sedimented on a black 96-well plate (Nunc, Waltham, Massachusetts, USA). Measurements were performed with a small-animal NIRF-imaging system (IVIS-200, Caliper Life Sciences, Hopkinton, Massachusetts, USA) using fluorescent filter sets of 515–665 nm for excitation, 695–770 nm for emission, and 580–610 nm for background subtraction with a 512 × 512-pixel matrix size

Copyright © 2015 John Wiley & Sons, Ltd.

(15 × 15 μm/pixel). Images were analysed semi-quantitatively by placing a region of interest (ROI) on individual wells. Total radiant efficiency was calculated with Living Image 4.2 software (Caliper Life Sciences).

5.4. NIRF imaging *in vivo*

Prior to NIRF imaging *in vivo*, 8–10-week-old mice were kept on an alfalfa-free diet for 7 days to reduce autofluorescence of the intestine. For generation of tumor xenografts of comparable size, mice were subcutaneously injected at their back on the right side with 1.5×10^6 ARTC2-transfected cells and on the left side with 0.5×10^6 untransfected cells in a mix of 0.1 mL RPMI medium and 0.1 mL Matrigel (BD Biosciences, Becton Dickinson, Franklin Lakes, USA). The different number of cells has been used to take into account the different growth rates of transfected and untransfected cells. After 7–9 days, when tumors reached ~8 mm in diameter, nanobody s+16a^{680} or conventional antibody Nika102^{680} was injected intravenously via the tail vein in a volume of 200 μL. NIRF imaging was performed before injection and 1, 2, 4, 6, 8, 12, and 24 h after injection. Initial studies showed that earlier time points did not yield useful diagnostic information due to high unspecific signals and were therefore not assessed. Experiments were performed with four doses of each AF680-conjugate: 5 μg, 10 μg, 25 μg, and 50 μg. This corresponded to 0.1 μg, 0.2 μg, 0.45 μg and 0.9 μg of injected dye for nanobody s+16a and 0.06 μg, 0.12 μg, 0.3 μg, and 0.6 μg of injected dye for monoclonal antibody Nika102.

For NIRF imaging *in vivo*, mice were anesthetized with isofluorane and positioned in the imaging chamber of the small-animal NIRF-imaging system using the same filter settings as described above. After qualitative imaging *in vivo*, quantitative analyses were performed by placing ROIs around the ARTC2-positive tumors, the ARTC2-negative tumors (negative control) and the hind limb (background signal). Even though the signal of the hind limb might underestimate the systemic background, we chose the hind limb because this tissue introduces less variation than abdominal organs or blood.

Total radiant efficiency was determined with Living Image 4.2 software (Caliper Life Sciences). Tumor-to-background ratio was calculated by dividing the tumor uptake value by the background value determined from the hind limb.

5.5. *Ex vivo* analyses

For *ex vivo* validation of *in vivo* measurements, animals were sacrificed 6 h or 24 h post-injection. ARTC2-positive and ARTC2-negative tumors and organs (spleen, lungs, liver, kidneys, stomach, ileum and muscle) were dissected. Biodistribution analysis was performed using NIRF imaging *ex vivo* as described by Bannas *et al*. (11). Total radiant efficiency of organs and tumors was determined and organ- and tumor-to-background ratio was calculated by dividing the tumor uptake value by the background value determined from explanted muscle tissue. Even though the signal of muscle might underestimate the systemic background, we chose muscle because this tissue introduces less variation than abdominal organs or blood.

For *ex vivo* fluorescence microscopy, one half of each harvested tumor was fixed in 4% paraformaldehyde over night, placed in 30% sucrose for 24 h and frozen on dry ice in Tissue-Tek® OCT™ (Sakura Finetek, Alphen, The Netherlands). Sections of 8 μm were prepared using a Reichert-Jung Ultracut microtome (Reichert-Jung, Wien, Austria). Tumor cryosections were stained with DAPI (Molecular Probes, Carlsbad, CA, USA) to visualize nuclei and CD31 (M-20, Santa Cruz, Heidelberg, Germany) to visualize vessels. Fluorescence microscopy analysis was performed using a Leica TCS SP5 confocal microscope (Leica Camera AG, Solms, Germany). A HeNe 633 nm laser was used for excitation of AlexaFluor680. Image analysis was performed using Leica LAS (Leica) and ImageJ software (NIH, USA).

For flow cytometry *ex vivo*, the other half of each tumor was dissected and passed through a 70 μm cell strainer to obtain single-cell suspensions. Dispersed cells were counterstained with pan leukocyte marker anti-CD45 (Clone 30-F1, eBioscience, San Diego, CA, USA) and Pacific Orange-NHS dye (Invitrogen, Grand Island, NY, USA) for live/dead staining. Labeling efficiency of ARTC2 by the injected AF680-conjugates was quantified by flow cytometry. For quantification of free circulating AF680-conjugates, serum was collected and used in a volume of 100 μL (1:100 dilution) for labeling 1×10^6 ARTC2-expressing DC27.10 cells with subsequent flow cytometry.

5.6. Statistical analysis

Data are presented as mean ± SD. Statistical analysis was performed using two-way ANOVA with Bonferroni's post-test analyses to evaluate differences between the two independent variables from experiments presented in Figs. 4 and 5. One-way ANOVA with Bonferroni's post-test analyses was performed to evaluate the significance of differences between four groups shown in Figs. 6 and 7A. $P < 0.05$ indicates statistical significance. Statistical analysis was performed using Prism 5, Graph Pad Software and Excel, Microsoft.

Acknowledgements

Parts of this work represent partial fulfillment of the requirements for the graduate thesis of Alexander Lenz at the University Hospital, Hamburg. This work was supported by the graduate school 'Inflammation and regeneration' of the Collaborative Research Centre 841 of the Deutsche Forschungsgemeinschaft (Alexander Lenz, Valentin Kunick), by the Collaborative Research Centre 877 of the Deutsche Forschungsgemeinschaft (Friedrich Koch-Nolte), by the Werner Otto Foundation (Peter Bannas), by the Wilhelm Sander Foundation (Peter Bannas, Friedrich Koch-Nolte), and by the Deutsche Forschungsgemeinschaft (Martin Trepel, Friedrich Haag and Friedrich Koch-Nolte).

REFERENCES

1. Hoffman JM, Gambhir SS. Molecular imaging: the vision and opportunity for radiology in the future. Radiology 2007; 244(1): 39–47.
2. Frangioni JV. New technologies for human cancer imaging. J Clin Oncol 2008; 26(24): 4012–4021.
3. Wu AM, Olafsen T. Antibodies for molecular imaging of cancer. Cancer J 2008; 14(3): 191–197.
4. Lisy MR, Goermar A, Thomas C, Pauli J, Resch-Genger U, Kaiser WA, Hilger I. *In vivo* near-infrared fluorescence imaging of carcinoembryonic antigen-expressing tumor cells in mice. Radiology 2008; 247(3): 779–787.
5. Wu AM. Antibodies and antimatter: the resurgence of immuno-PET. J Nucl Med 2009; 50(1): 2–5.
6. Kaur S, Venktaraman G, Jain M, Senapati S, Garg PK, Batra SK. Recent trends in antibody-based oncologic imaging. Cancer Lett 2012; 315(2): 97–111.
7. Kelloff GJ, Krohn KA, Larson SM, Weissleder R, Mankoff DA, Hoffman JM, Link JM, Guyton KZ, Eckelman WC, Scher HI, O'Shaughnessy J, Cheson BD, Sigman CC, Tatum JL, Mills GQ, Sullivan DC, Woodcock

 Copyright © 2015 John Wiley & Sons, Ltd.

J. The progress and promise of molecular imaging probes in oncologic drug development. Clin Cancer Res 2005; 11(22): 7967–7985.
8. Holliger P, Hudson PJ. Engineered antibody fragments and the rise of single domains. Nat Biotechnol 2005; 23(9): 1126–1136.
9. Hamers-Casterman C, Atarhouch T, Muyldermans S, Robinson G, Hamers C, Songa EB, Bendahman N, Hamers R. Naturally occurring antibodies devoid of light chains. Nature 1993; 363(6428): 446–448.
10. Wesolowski J, Alzogaray V, Reyelt J, Unger M, Juarez K, Urrutia M, Cauerhff A, Danquah W, Rissiek B, Scheuplein F, Schwarz N, Adriouch S, Boyer O, Seman M, Licea A, Serreze DV, Goldbaum FA, Haag F, Koch-Nolte F. Single domain antibodies: promising experimental and therapeutic tools in infection and immunity. Med Microbiol Immunol 2009; 198(3): 157–174.
11. Bannas P, Well L, Lenz A, Rissiek B, Haag F, Schmid J, Hochgrafe K, Trepel M, Adam G, Ittrich H, Koch-Nolte F. *In vivo* near-infrared fluorescence targeting of T cells: comparison of nanobodies and conventional monoclonal antibodies. Contrast Media Mol Imaging 2014; 9(2): 135–142.
12. Vaneycken I, Devoogdt N, Van Gassen N, Vincke C, Xavier C, Wernery U, Muyldermans S, Lahoutte T, Caveliers V. Preclinical screening of anti-HER2 nanobodies for molecular imaging of breast cancer. FASEB J 2011; 25(7): 2433–2446.
13. Xavier C, Vaneycken I, D'Huyvetter M, Heemskerk J, Keyaerts M, Vincke C, Devoogdt N, Muyldermans S, Lahoutte T, Caveliers V. Synthesis, preclinical validation, dosimetry, and toxicity of 68Ga-NOTA-anti-HER2 Nanobodies for iPET imaging of HER2 receptor expression in cancer. J Nucl Med 2013; 54(5): 776–784.
14. Tchouate Gainkam LO, Keyaerts M, Caveliers V, Devoogdt N, Vanhove C, Van Grunsven L, Muyldermans S, Lahoutte T. Correlation between epidermal growth factor receptor-specific nanobody uptake and tumor burden: a tool for noninvasive monitoring of tumor response to therapy. Mol Imaging Biol 2011; 13(5): 940–948.
15. Vosjan MJ, Perk LR, Roovers RC, Visser GW, Stigter-van Walsum M. van Bergen En Henegouwen PM, van Dongen GA. Facile labelling of an anti-epidermal growth factor receptor Nanobody with 68Ga via a novel bifunctional desferal chelate for immuno-PET. Eur J Nucl Med Mol Imaging 2011; 38(4): 753–763.
16. Oliveira S, Heukers R, Sornkom J, Kok RJ, van Bergen En Henegouwen PM. Targeting tumors with nanobodies for cancer imaging and therapy. J Control Release 2013; 172(3): 607–617.
17. Kijanka M, Warnders FJ, El Khattabi M, Lub-de Hooge M, van Dam GM, Ntziachristos V, de Vries L, Oliveira S. van Bergen En Henegouwen PM. Rapid optical imaging of human breast tumour xenografts using anti-HER2 VHHs site-directly conjugated to IRDye 800CW for image-guided surgery. Eur J Nucl Med Mol Imaging 2013; 40(11): 1718–1729.
18. Zaman MB, Baral TN, Jakubek ZJ, Zhang J, Wu X, Lai E, Whitfield D, Yu K. Single-domain antibody bioconjugated near-IR quantum dots for targeted cellular imaging of pancreatic cancer. J Nanosci Nanotechnol 2011; 11(5): 3757–3763.
19. Oliveira S, van Dongen GA, Stigter-van Walsum M, Roovers RC, Stam JC, Mali W, van Diest PJ, van Bergen en Henegouwen PM. Rapid visualization of human tumor xenografts through optical imaging with a near-infrared fluorescent anti-epidermal growth factor receptor nanobody. Mol Imaging 2012; 11(1): 33–46.
20. D'Huyvetter M, Vincke C, Xavier C, Aerts A, Impens N, Baatout S, De Raeve H, Muyldermans S, Caveliers V, Devoogdt N, Lahoutte T. Targeted radionuclide therapy with A 177Lu-labeled anti-HER2 nanobody. Theranostics 2014; 4(7): 708–720.
21. Mould DR, Sweeney KR. The pharmacokinetics and pharmacodynamics of monoclonal antibodies--mechanistic modeling applied to drug development. Curr Opin Drug Discov Develop 2007; 10(1): 84–96.
22. Lammers T, Kiessling F, Hennink WE, Storm G. Drug targeting to tumors: principles, pitfalls and (pre-) clinical progress. J Control Release 2012; 161(2): 175–187.
23. Jain RK, Stylianopoulos T. Delivering nanomedicine to solid tumors. Nature Rev Clin Oncol 2010; 7(11): 653–664.
24. Koch-Nolte F, Duffy T, Nissen M, Kahl S, Killeen N, Ablamunits V, Haag F, Leiter EH. A new monoclonal antibody detects a developmentally regulated mouse ecto-ADP-ribosyltransferase on T cells: subset distribution, inbred strain variation, and modulation upon T cell activation. J Immunol 1999; 163(11): 6014–6022.
25. Koch-Nolte F, Reyelt J, Schossow B, Schwarz N, Scheuplein F, Rothenburg S, Haag F, Alzogaray V, Cauerhff A, Goldbaum FA. Single domain antibodies from llama effectively and specifically block T cell ecto-ADP-ribosyltransferase ART2.2 *in vivo*. FASEB J 2007; 21(13): 3490–3498.
26. Bannas P, Adriouch S, Kahl S, Braasch F, Haag F, Koch-Nolte F. Activity and specificity of toxin-related mouse T cell ecto-ADP-ribosyltransferase ART2.2 depends on its association with lipid rafts. Blood 2005; 105(9): 3663–3670.
27. Bannas P, Graumann O, Balcerak P, Peldschus K, Kaul MG, Hohenberg H, Haag F, Adam G, Ittrich H, Koch-Nolte F. Quantitative magnetic resonance imaging of enzyme activity on the cell surface: *in vitro* and *in vivo* monitoring of ADP-ribosyltransferase 2 on T cells. Mol Imaging 2010; 9(4): 211–222.
28. Bannas P, Scheuplein F, Well L, Hermans-Borgmeyer I, Haag F, Koch-Nolte F. Transgenic overexpression of toxin-related ecto-ADP-ribosyltransferase ART2.2 sensitizes T cells but not B cells to NAD-induced cell death. Mol Immunol 2011; 48(15–16): 1762–1770.
29. Hottiger MO, Hassa PO, Luscher B, Schuler H, Koch-Nolte F. Toward a unified nomenclature for mammalian ADP-ribosyltransferases. Trends Biochem Sci 2010; 35(4): 208–219.
30. Gainkam LO, Caveliers V, Devoogdt N, Vanhove C, Xavier C, Boerman O, Muyldermans S, Bossuyt A, Lahoutte T. Localization, mechanism and reduction of renal retention of technetium-99 m labeled epidermal growth factor receptor-specific nanobody in mice. Contrast Media Mol Imaging 2011; 6(2): 85–92.

SUPPORTING INFORMATION

Additional supporting information may be found in the online version of this article at the publisher's web site.

Copyright © 2015 John Wiley & Sons, Ltd.